

RF Tomography for Below-Ground Imaging of Extended Areas and Close-in Sensing

Lorenzo Lo Monte, *Member, IEEE*, Danilo Erricolo, *Senior Member, IEEE*,
 Francesco Soldovieri, and Michael C. Wicks, *Fellow, IEEE*

Abstract—Three extensions to radio-frequency (RF) tomography for imaging of voids under wide areas of regard are presented. These extensions are motivated by three challenges. One challenge is the lateral wave, which propagates in proximity of the air–earth interface and represents the predominant radiation mechanism for wide-area surveillance, sensing of denied terrain, or close-in sensing. A second challenge is the direct-path coupling between transmitters (Tx) and receivers (Rx), that affects the measurements. A third challenge is the generation of clutter by the unknown distribution of anomalies embedded in the ground. These challenges are addressed and solved using the following strategies: 1) A forward model for RF tomography that accounts for lateral waves expressed in closed form (for fast computation); 2) a strategy that reduces the direct-path coupling between any Tx–Rx pair; and 3) an improved inversion scheme that is robust with respect to noise, clutter, and high attenuation. A finite-difference time domain simulation of a scenario representing close-in sensing of a denied area is performed, and reconstructed images obtained using the improved and the classical models of RF tomography are compared.

Index Terms—Green’s functions, ground-penetrating radar, lateral waves, radio-frequency tomography, tunnel detection.

I. INTRODUCTION

THE PROBLEM of underground void detection is paramount to secure borders and sensitive areas and for search and rescue missions. To date, no underground imaging technique emerged as a standard for close-in sensing of wide denied areas, where minimal human intervention is required [1].

A promising strategy is introduced in [1] and [2] where a set of transmitters (Tx) and a set of receivers (Rx) are placed on (or in) the ground at *arbitrary* positions. The Tx radiate a monochromatic signal, which impinges upon a buried dielectric or conductive anomaly, thus generating a scattered field. Multiple Rx collect samples of the scattered electric field and relay this information to a base station. Images of the below-ground scene are then reconstructed using the principles of *RF tomography*. The advantages and mathematical

derivations of RF tomography for underground imaging are discussed in [1]. The approach is technically valid for any sensor disposition and terrain shape provided that the Green’s function characterizing the problem is properly selected. In [1], the Green’s function for a homogeneous space was applied due to its simplicity of implementation. This choice has been proven to work satisfactorily when the sensors and targets are located nearly vertically above the targets, thus avoiding artifacts due to the discontinuity at the air–earth interface.

However, practical applications require wide areas of investigations (e.g., underground networks and facilities), denied areas (e.g., sensing of urban environment), or close-in sensing. In these cases, sensors remotely probe underground regions at long ranges, and the propagation of waves occurs primarily along the air/ground interface; hence, the predominant propagation mode is the *lateral wave* [8]–[10]. Therefore, one contribution of this letter is the introduction of a more accurate forward model by invoking a closed-form Green’s function that accounts for the air–earth discontinuity (see Appendix).

In addition, RF tomography is based upon the knowledge of the scattered field from targets. In real cases, the Rx are irradiated by a strong electromagnetic field due to the direct coupling between each Tx and Rx pair (i.e., *direct-path coupling* [1]). Hence, as a second contribution, in Section III, an efficient technique that mitigates the direct-path coupling (by joint Tx and Rx null steering) is presented.

Moreover, distributed anomalies (e.g., weathered soils) also generate a bias to the measured scattered field, which may be considered as *clutter*. A third contribution, given in Section IV, is an improvement upon the inversion schemes already discussed in literature [3]–[5], based on the findings described by Zhdanov [7] from the geophysical community; this improved method is more robust with respect to perturbations (e.g., clutter) of the measured scattered field.

The combination of these three new strategies improves the image-reconstruction process, particularly for large areas of interest, shallow targets, and close-in sensing, as shown in Section V.

II. FORWARD MODEL

The 3-D geometry shown in Fig. 1 is considered. Under the monochromatic assumption (single work frequency f), the air half-space is modeled as a free-space medium, while the ground half-space is modeled as a homogeneous medium with relative dielectric permittivity ϵ_D , conductivity σ_D , and magnetic permeability μ_0 . The targets (i.e., tunnels, caches, or voids) are

Manuscript received May 21, 2009; revised September 10, 2009. Date of publication March 1, 2010; date of current version April 29, 2010. This work was supported in part by the Air Force Research Laboratory under Contract F33601-02-F-A581 and in part by the U.S. Department of Defense under Grant FA9550-05-1-0443.

L. Lo Monte is with General Dynamics Information Technology, Dayton, OH 45431 USA (e-mail: lorenzo.lomonte@gdit.com).

D. Erricolo is with the University of Illinois at Chicago, Chicago, IL 60607 USA (e-mail: erricolo@ece.uic.edu).

F. Soldovieri is with the Istituto per il Rilevamento Elettromagnetico dell’Ambiente–CNR, 80124 Naples, Italy (e-mail: soldovieri.f@irea.cnr.it).

M. C. Wicks is with the Sensors Directorate, Air Force Research Laboratory, Rome, NY 13441 USA (e-mail: michael.wicks@rl.af.mil).

Digital Object Identifier 10.1109/LGRS.2009.2039918

Report Documentation Page				Form Approved OMB No. 0704-0188	
Public reporting burden for the collection of information is estimated to average 1 hour per response, including the time for reviewing instructions, searching existing data sources, gathering and maintaining the data needed, and completing and reviewing the collection of information. Send comments regarding this burden estimate or any other aspect of this collection of information, including suggestions for reducing this burden, to Washington Headquarters Services, Directorate for Information Operations and Reports, 1215 Jefferson Davis Highway, Suite 1204, Arlington VA 22202-4302. Respondents should be aware that notwithstanding any other provision of law, no person shall be subject to a penalty for failing to comply with a collection of information if it does not display a currently valid OMB control number.					
1. REPORT DATE 10 SEP 2009		2. REPORT TYPE		3. DATES COVERED 00-00-2009 to 00-00-2009	
4. TITLE AND SUBTITLE RF Tomography for Below-Ground Imaging of Extended Areas and Close-in Sensing				5a. CONTRACT NUMBER	
				5b. GRANT NUMBER	
				5c. PROGRAM ELEMENT NUMBER	
6. AUTHOR(S)				5d. PROJECT NUMBER	
				5e. TASK NUMBER	
				5f. WORK UNIT NUMBER	
7. PERFORMING ORGANIZATION NAME(S) AND ADDRESS(ES) Air Force Research Laboratory,Sensors Directorate,Rome,NY,13441				8. PERFORMING ORGANIZATION REPORT NUMBER	
9. SPONSORING/MONITORING AGENCY NAME(S) AND ADDRESS(ES)				10. SPONSOR/MONITOR'S ACRONYM(S)	
				11. SPONSOR/MONITOR'S REPORT NUMBER(S)	
12. DISTRIBUTION/AVAILABILITY STATEMENT Approved for public release; distribution unlimited					
13. SUPPLEMENTARY NOTES					
14. ABSTRACT Three extensions to radio-frequency (RF) tomography for imaging of voids under wide areas of regard are presented. These extensions are motivated by three challenges. One challenge is the lateral wave, which propagates in proximity of the air?earth interface and represents the predominant radiation mechanism for wide-area surveillance, sensing of denied terrain or close-in sensing. A second challenge is the direct-path coupling between transmitters (Tx) and receivers (Rx), that affects the measurements. A third challenge is the generation of clutter by the unknown distribution of anomalies embedded in the ground. These challenges are addressed and solved using the following strategies: 1) A forward model for RF tomography that accounts for lateral waves expressed in closed form (for fast computation) 2) a strategy that reduces the direct-path coupling between any Tx?Rx pair; and 3) an improved inversion scheme that is robust with respect to noise, clutter, and high attenuation. A finitedifference time domain simulation of a scenario representing close-in sensing of a denied area is performed, and reconstructed images obtained using the improved and the classicalmodels of RF tomography are compared.					
15. SUBJECT TERMS					
16. SECURITY CLASSIFICATION OF:			17. LIMITATION OF ABSTRACT	18. NUMBER OF PAGES	19a. NAME OF RESPONSIBLE PERSON
a. REPORT unclassified	b. ABSTRACT unclassified	c. THIS PAGE unclassified			

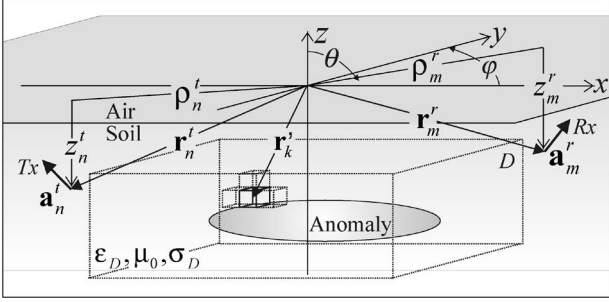


Fig. 1. Three-dimensional geometry for the model.

assumed to reside in the investigation domain D . The sources are N electrically small dipoles (of length Δl) fed with current I . For each transmitting sensor, the total field \mathbf{E} is collected by M Rx's. Both Tx's and Rx's reside inside the ground but outside the investigation domain D . The relative dielectric permittivity $\varepsilon_r(\mathbf{r}')$ and the conductivity $\sigma(\mathbf{r}')$ inside D are the unknowns of this problem. The *contrast* function is defined as [1]

$$\varepsilon_\delta(\mathbf{r}') = \varepsilon_r(\mathbf{r}') - \varepsilon_D + j(\sigma(\mathbf{r}') - \sigma_D) / 2\pi f \varepsilon_0 \quad (1)$$

being ε_0 the free-space dielectric permittivity. However, other definitions may be used [3]–[5], [8]. By pointing out the first order *Born approximation* [3]–[5], [7], [8], the field received by a dipole oriented along the direction \mathbf{a}_m^r , positioned at \mathbf{r}_m^r due to a transmitting dipole oriented along the direction \mathbf{a}_n^t , positioned at \mathbf{r}_n^t , can be written as [1]

$$\begin{aligned} E(\mathbf{r}_m^r, \mathbf{r}_n^t) &= Q \mathbf{a}_m^r \cdot \underline{\mathbf{G}}(\mathbf{r}_m^r, \mathbf{r}_n^t) \cdot \mathbf{a}_n^t + H(\mathbf{r}_m^r, \mathbf{r}_n^t) + T \\ &+ Q k_0^2 \int \int \int_D [\mathbf{a}_m^r \cdot \underline{\mathbf{G}}(\mathbf{r}_m^r, \mathbf{r}')] \cdot [\underline{\mathbf{G}}(\mathbf{r}', \mathbf{r}_n^t) \cdot \mathbf{a}_n^t] \varepsilon_\delta(\mathbf{r}') d\mathbf{r}' \end{aligned} \quad (2)$$

where $Q = j\omega\mu_0\Delta l I$ for an electrically small dipole [3]; the quantities H (multiple scattering) and T (random noise) represent unpredictable perturbations to the total field. $\underline{\mathbf{G}}$ is the Green's dyadic, to be chosen according to the adopted formulation. The first term in (2), i.e.,

$$Q \mathbf{a}_m^r \cdot \underline{\mathbf{G}}(\mathbf{r}_m^r, \mathbf{r}_n^t) \cdot \mathbf{a}_n^t \quad (3)$$

describes the direct-path coupling between a particular Tx and Rx pair. The cancellation of this coupling from the measured field is a critical problem in RF tomography: Although it can be analytically predicted (and cancelled) using (3), in practical cases, its magnitude may be up to 50–60 dB higher than the scattered signal. In these conditions, the dynamic range of the Rx's amplifiers may not be large enough, or the quantization steps may not be as fine as required, to sample both scattered and direct-path coupling fields accordingly. Clearly, the best solution is to cancel the direct-path contribution *before* it reaches the Rx.

III. DIRECT-PATH-COUPLING MITIGATION

In this section, a direct-path coupling mitigation technique is introduced. The key feature is the possibility to steer the Tx and

Rx dipoles toward the desired directions. Rotation of dipoles may be performed using mechanical devices or by properly feeding a set of colocated orthogonal dipoles (see [1]). The proposed strategy properly steers the Tx dipole in order to minimize the field at the Rx side, and then turns the Rx dipole in order to be orthogonal to the expected direct-path electric field. Mathematically, these rotations are computed by solving a series of constrained minimization problems for each Tx and Rx pair

$$\text{minimize } \|\underline{\mathbf{G}}(\mathbf{r}_m^r, \mathbf{r}_n^t) \cdot \mathbf{a}_n^t\|_2^2 \quad \text{subject to } (\mathbf{a}_n^t)^T \cdot \mathbf{a}_n^t = 1. \quad (4)$$

In Lagrangian form, it becomes

$$\begin{aligned} \Lambda_{n,m}(\mathbf{a}_n^t, \lambda) &= (\mathbf{a}_n^t)^T \cdot \underline{\mathbf{G}}^H(\mathbf{r}_m^r, \mathbf{r}_n^t) \cdot \underline{\mathbf{G}}(\mathbf{r}_m^r, \mathbf{r}_n^t) \cdot \mathbf{a}_n^t \\ &- \lambda [(\mathbf{a}_n^t)^T \cdot \mathbf{a}_n^t - 1] \end{aligned} \quad (5)$$

where $\underline{\mathbf{G}}^H$ denotes the Hermitian of $\underline{\mathbf{G}}$. By imposing $\nabla \Lambda_{n,m} = 0$ we obtain

$$\underline{\mathbf{G}}^H(\mathbf{r}_m^r, \mathbf{r}_n^t) \cdot \underline{\mathbf{G}}(\mathbf{r}_m^r, \mathbf{r}_n^t) \cdot \mathbf{a}_n^t = \lambda \mathbf{a}_n^t. \quad (6)$$

Therefore, the \mathbf{a}_n^t direction that minimizes the power at a desired location is the eigenvector associated with the *smallest* eigenvalue of the matrix $\underline{\mathbf{G}}^H \underline{\mathbf{G}}$. Similarly, this minimization can be applied at the Rx side. Defining the vector

$$\mathbf{E}_{\min} = \underline{\mathbf{G}}(\mathbf{r}_m^r, \mathbf{r}_n^t) \cdot \mathbf{a}_n^t \quad (7)$$

as the electric field obtained when \mathbf{a}_n^t is chosen according to (4), a second minimization problem can be formulated as

$$\text{minimize } \|(\mathbf{a}_m^r)^T \cdot \mathbf{E}_{\min}\|_2^2 \quad \text{subject to } (\mathbf{a}_m^r)^T \cdot \mathbf{a}_m^r = 1. \quad (8)$$

The minimization is achieved when \mathbf{a}_m^r is chosen to be the eigenvector corresponding to the smallest eigenvalue of the outer product (matrix) $\mathbf{E}_{\min} \cdot (\mathbf{E}_{\min})^T$. If the dipole can be steered only over a horizontal plane (e.g., by using two crossed dipoles), the steering directions are easily obtained by setting to zero the z -component of each vector \mathbf{a}_n .

As tested via numerical analysis, the application of these strategies guarantees an acceptable minimization of the received signal due to direct-path coupling. Therefore, the total electric field can be reasonably approximated only with the first-order scattered contribution from targets inside the region D , i.e., [3]

$$\begin{aligned} E(\mathbf{r}_m^r, \mathbf{r}_n^t) &\cong \mathbf{L}(\varepsilon_\delta(\mathbf{r}')) \\ &= Q k_0^2 \times \int \int \int_D [\mathbf{a}_m^r \cdot \underline{\mathbf{G}}(\mathbf{r}_m^r, \mathbf{r}')] \\ &\quad \cdot [\underline{\mathbf{G}}(\mathbf{r}', \mathbf{r}_n^t) \cdot \mathbf{a}_n^t] \varepsilon_\delta(\mathbf{r}') d\mathbf{r}'. \end{aligned} \quad (9)$$

IV. INVERSION

Assuming that the clutter contribution has been completely mitigated and the field received by the sensors is given by the forward model in (9), the sampled field at each Tx and Rx pair can be collected in a vector $\mathbf{e} = \{E(\mathbf{r}_n^t, \mathbf{r}_m^r)\}$, and the

investigation region D can be discretized in K voxels, each one located at position \mathbf{r}'_k . The contrast function can be represented in a column vector $\boldsymbol{\varepsilon} = \{\varepsilon_\delta(\mathbf{r}'_k)\}$. After this discretization, (9) can be reformulated in matrix form, i.e.,

$$\mathbf{e} = \mathbf{L} \cdot \boldsymbol{\varepsilon} \quad (10)$$

where \mathbf{L} is generally an ill-conditioned matrix.

Several methods have been proposed to solve (10), such as back propagation [1], truncated singular-value decomposition (SVD) [4], [11], and Tikhonov regularization [7], [11]. In this letter, we introduce a refined version of Tikhonov regularization that equalizes the sensitivity of each Tx and Rx pair by selecting a proper weighting factor and introduces a term that is able to exploit the *a priori* information on the values of the dielectric anomalies. Accordingly, the contrast function (as a function of the regularization parameter β) can be estimated [7]

$$\hat{\boldsymbol{\varepsilon}}(\beta) = (\mathbf{L}^H \mathbf{W}_E^2 \mathbf{L} + \beta \mathbf{W}_\varepsilon^2)^{-1} (\mathbf{L}^H \mathbf{W}_E^2 \cdot \mathbf{e} + \beta \mathbf{W}_\varepsilon^2 \boldsymbol{\varepsilon}^0) \quad (11)$$

where $\boldsymbol{\varepsilon}^0$ represents the known dielectric anomalies embedded in region D , and

$$\mathbf{W}_\varepsilon = \text{diag}(\mathbf{L}^H \mathbf{L})^{1/2} \quad \mathbf{W}_E = \text{diag}(\mathbf{L} \mathbf{L}^H)^{1/2} \quad (12)$$

are (diagonal) weighting matrices opportunely defined in order to minimize the sensitivity of the system [7].

In most cases, the weighting matrices have a small dynamic range. Therefore, we can approximate $\mathbf{W}_\varepsilon \cong \alpha \mathbf{I}$ in (11). If we perform the SVD [11] of a properly defined weighed matrix $\mathbf{L}_w = \mathbf{W}_E \mathbf{L} = \mathbf{U} \mathbf{S} \mathbf{V}^H$, (11) becomes

$$\begin{aligned} \hat{\boldsymbol{\varepsilon}} &= (\mathbf{L}_w^H \mathbf{L}_w + \beta \mathbf{W}_\varepsilon^2)^{-1} (\mathbf{L}_w^H \mathbf{W}_E \cdot \mathbf{e} + \beta \mathbf{W}_\varepsilon^2 \boldsymbol{\varepsilon}^0) \\ &\cong (\mathbf{V} \mathbf{S}^H \mathbf{S} \mathbf{V}^H + \alpha^2 \beta \mathbf{I})^{-1} (\mathbf{V} \mathbf{S}^H \mathbf{U}^H \mathbf{W}_E \cdot \mathbf{e} + \beta \mathbf{W}_\varepsilon^2 \boldsymbol{\varepsilon}^0) \\ &= \mathbf{V} \text{diag}(s_i^2 + \alpha^2 \beta)^{-1} (\mathbf{S}^H \mathbf{U}^H \mathbf{W}_E \cdot \mathbf{e} + \beta \mathbf{V}^H \mathbf{W}_\varepsilon^2 \boldsymbol{\varepsilon}^0) \end{aligned} \quad (13)$$

where s_i represents the i th singular value of \mathbf{L}_w . The advantage obtained in applying (13) is that the contrast function as function of β can be computed via (fast) matrix multiplications.

V. SIMULATIONS AND CONCLUSION

A simulation is presented in order to demonstrate the improvements achieved by using the following: 1) lateral waves in the forward model; 2) direct-path mitigation; and 3) weighted Tikhonov regularization. The test scene represents a situation where sensors are surrounding the wide (denied) area of interest (i.e., close-in sensing) and probe the region D mostly via lateral waves (see Fig. 2 for details).

The targets are two hollow cylinders (radius 1 m) emulating two tunnels, located with their axes parallel to the surface and at a depth $z' = -5$ m (with respect to their center), having $\varepsilon_D = 9$ and $\sigma_D = 5 \times 10^{-4}$ S/m. No *a priori* information about dielectric anomalies in the scene is considered, thus $\boldsymbol{\varepsilon}^0 = 0$. The work frequency is 5 MHz. Placed along a circle encompassing the two tunnels are 12 Tx and 20 Rx, as shown in Fig. 2. Each sensor is emplaced at depth $d = 0.25$ m beneath the surface.

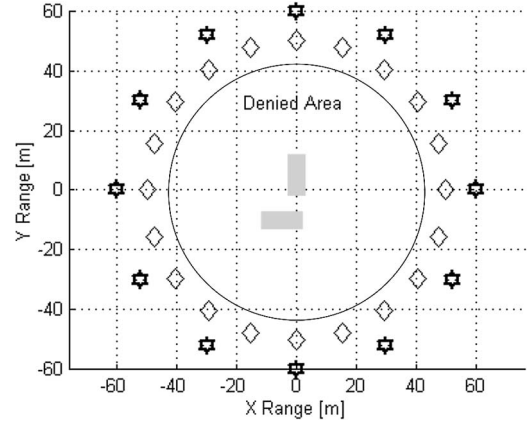


Fig. 2. Geometry for the simulation. Tx and Rx are indicated with stars and diamonds, respectively, and the two tunnels are located at the center of the scene.

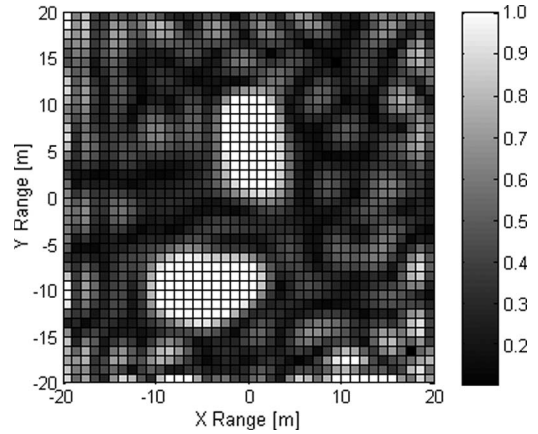


Fig. 3. Reconstructed image using homogeneous Green's function. Depth slice: 5 m.

The received electric field has been synthesized using the finite-difference time domain simulator GPRMAX [6] for each Tx and Rx pair.

In the first simulation, the process was as follows: 1) The homogeneous Green's function [8], [9], having the properties of the soil, is inserted in the forward model; 2) the truncated SVD method [1], [4] is used for the inversion; and 3) the direct-path coupling is assumed to be completely cancelled. The reconstruction result is shown in Fig. 3.

In the second simulation, the procedure was as follows: 1) The closed-form Green's function that accounts for the lateral wave (see Appendix) was used; 2) the weighted Tikhonov method proposed in Section IV was implemented; and 3) the direct-path-mitigation algorithm (Section III) was used to choose the direction of each sensor. The reconstruction result is shown in Fig. 4.

As expected, the shallow targets are mainly irradiated by the lateral wave excited at the air–earth interface, and the classical Green's function for the homogeneous space cannot accurately predict the field value. Conversely, the half-space Green's function generates highly resolved images, particularly for shallow targets since it accounts for the effects of lateral wave (see Fig. 4). Therefore, we conclude that when RF tomography is applied in wide areas, denied terrain, or when targets

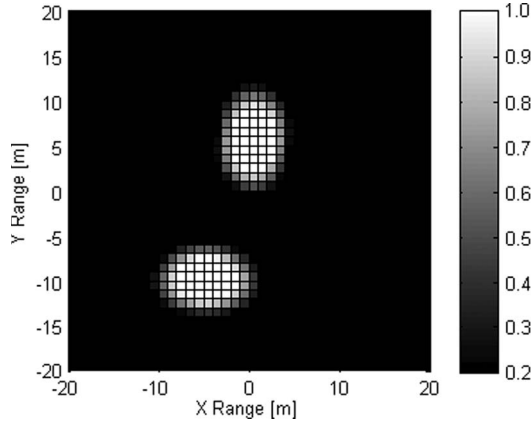


Fig. 4. Reconstructed image using half-space Green's function described in the Appendix. Depth slice: 5 m.

are in shallow regions, the discussed improvements (i.e., the inclusion of the lateral waves propagation within the realm of RF tomography and its fast numerical computation, the direct-path coupling suppression using steerable radiators, and the improved inversion scheme for better handling the clutter) are a suitable choice to obtain high-quality reconstructions.

APPENDIX HALF SPACE GREEN'S FUNCTION

Half-space Green's functions have been proposed in the literature [3], [5], [9], [11], but they are generally expressed as asymptotic expansions or in spectral form. Nevertheless, King *et al.* [10] derived explicit closed-form expressions for the electric field generated by horizontal and vertical dipoles buried in a lossy medium [under assumption reported in (16)]. From King's formulas, a closed-form expression for the half-space Green's function is derived (valid only when antennas and targets are embedded in the soil).

A dyadic Green's function can be expressed as follows:

$$\underline{\mathbf{G}}(\mathbf{r}, \mathbf{r}') = -\frac{j}{4\pi k_D^2} \begin{bmatrix} g_{XX} & g_{XY} & g_{XZ} \\ g_{YX} & g_{YY} & g_{YZ} \\ g_{ZX} & g_{ZY} & g_{ZZ} \end{bmatrix}. \quad (14)$$

In this case, $\mathbf{r} = x\hat{\mathbf{x}} + y\hat{\mathbf{y}} + z\hat{\mathbf{z}}$ represents the observation point, and $\mathbf{r}' = x'\hat{\mathbf{x}} + y'\hat{\mathbf{y}} + z'\hat{\mathbf{z}}$ represents the current (physical or equivalent) source position. The coefficients in (14) are given as

$$\begin{aligned} g_{XX} &= g_\rho^h \cos^2 \varphi - g_\varphi^h \sin^2 \varphi & g_{XY} &= (g_\rho^h + g_\varphi^h) \sin \varphi \cos \varphi \\ g_{XZ} &= -g_\rho^v \cos \varphi & g_{YX} &= (g_\rho^h + g_\varphi^h) \cos \varphi \sin \varphi \\ g_{YY} &= g_\rho^h \sin^2 \varphi - g_\varphi^h \cos^2 \varphi & g_{YZ} &= -g_\rho^v \sin \varphi \\ g_{ZX} &= -g_z^h \cos \varphi & g_{ZY} &= -g_z^h \sin \varphi & g_{ZZ} &= g_z^v. \end{aligned}$$

Using the following notation (see Fig. 1)

$$\begin{aligned} k_0 &= \omega \sqrt{\mu_0 \varepsilon_0} & k_D &= \omega \sqrt{\mu_0 \varepsilon_0 \varepsilon_D} \\ \rho &= \sqrt{(x - x')^2 + (y - y')^2} & \varphi &= \arctan \left[\frac{y - y'}{x - x'} \right] \\ r_d &= |\mathbf{r} - \mathbf{r}'| = \sqrt{\rho^2 + (z - z')^2} & r_i &= \sqrt{\rho^2 + (z + z')^2} \end{aligned}$$

the Green's function coefficients are expressed as follows:

$$\begin{aligned} g_\rho^h &= e^{jk_D r_d} \left[\frac{2k_D}{r_d^2} + \frac{2j}{r_d^3} + \frac{(z - z')^2}{r_d^2} \right. \\ &\quad \times \left(\frac{jk_D^2}{r_d} - \frac{3k_D}{r_d^2} - \frac{3j}{r_d^3} \right) \Big] \\ &\quad + e^{jk_D r_i} \left[\frac{2k_D}{r_i^2} + \frac{2j}{r_i^3} + \frac{(z + z')^2}{r_i^2} \right. \\ &\quad \times \left(\frac{jk_D^2}{r_i} - \frac{3k_D}{r_i^2} - \frac{3j}{r_i^3} \right) \Big] \\ &\quad - 2e^{jk_D r_i} \left[\frac{k_D}{r_i^2} + \frac{j}{r_i^3} - \left(\frac{z + z'}{\rho} \right) \left(\frac{jk_D}{\rho^2} - \frac{3}{2\rho^3} \right) \right] \\ &\quad - 2k_0 \left[\frac{jk_0}{\rho} - \frac{1}{\rho^2} - \frac{j}{k_0 \rho^3} - \frac{k_0^3}{k_D} \right. \\ &\quad \times \left(\frac{\pi}{k_0 \rho} \right)^{1/2} e^{-jp} F(p) \Big] e^{-jk_D(z+z')} e^{jk_0 \rho} \\ g_\varphi^h &= -e^{jk_D r_d} \left(\frac{jk_D^2}{r_d} - \frac{k_D}{r_d^2} - \frac{j}{r_d^3} \right) \\ &\quad - e^{jk_D r_i} \left(\frac{jk_D^2}{r_i} - \frac{k_D}{r_i^2} - \frac{j}{r_i^3} \right) \\ &\quad + 4e^{jk_D r_i} \left(\frac{jk_D^2}{2r_i} - \frac{k_D}{r_i^2} - \frac{j}{r_i^3} \right) \\ &\quad + 2e^{jk_D r_i} \left(\frac{z + z'}{r_i} \right) \left(\frac{k_D^2}{\rho} + \frac{3jk_D}{2\rho^2} - \frac{5}{8\rho^3} \right) \\ &\quad - 2e^{jk_D r_i} \left(\frac{z + z'}{r_i} \right)^2 \left(\frac{jk_D^2}{r_i} - \frac{3k_D}{r_i^2} - \frac{3j}{r_i^3} \right) \\ &\quad + 4e^{-jk_D(z+z')} e^{jk_0 \rho} \\ &\quad \times \left[\frac{k_0}{\rho^2} + \frac{j}{\rho^3} + \frac{jk_0^3}{2k_D \rho} \left(\frac{\pi}{k_0 \rho} \right)^{1/2} e^{-jp} F(p) \right] \\ g_z^h &= -e^{jk_D r_d} \left(\frac{\rho}{r_d} \right) \left(\frac{z - z'}{r_d} \right) \left(\frac{jk_D^2}{r_d} - \frac{3k_D}{r_d^2} - \frac{3j}{r_d^3} \right) \\ &\quad - e^{jk_D r_i} \left(\frac{\rho}{r_i} \right) \left(\frac{z + z'}{r_i} \right) \left(\frac{jk_D^2}{r_i} - \frac{3k_D}{r_i^2} - \frac{3j}{r_i^3} \right) \\ &\quad + \frac{2jk_0^2}{k_D} e^{jk_D r_i} \left(\frac{1}{\rho^2} - \frac{3j}{2k_D \rho^3} \right) \\ &\quad - \frac{2jk_0^2}{k_D} e^{-jk_D(z+z')} e^{jk_0 \rho} \\ &\quad \times \left(\frac{k_0}{\rho} + \frac{j}{\rho^2} + \frac{jk_0^3}{k_D} \left(\frac{\pi}{k_0 \rho} \right)^{1/2} e^{-jp} F(p) \right) \\ g_\rho^v &= -e^{jk_D r_d} \left(\frac{jk_D^2}{r_d} - \frac{3k_D}{r_d^2} - \frac{3j}{r_d^3} \right) \left(\frac{\rho}{r_d} \right) \left(\frac{z - z'}{r_d} \right) \\ &\quad + e^{jk_D r_i} \left(\frac{jk_D^2}{r_i} - \frac{3k_D}{r_i^2} - \frac{3j}{r_i^3} \right) \left(\frac{\rho}{r_i} \right) \left(\frac{z + z'}{r_i} \right) \\ &\quad + \frac{2jk_0^2}{k_D} e^{jk_D r_i} \left(\frac{1}{\rho^2} + \frac{3j}{2k_D \rho^3} \right) \\ &\quad - \frac{2k_0^2}{k_D} e^{-jk_D(z+z')} e^{jk_0 \rho} \\ &\quad \times \left(\frac{jk_0}{\rho} - \frac{1}{\rho^2} - \frac{k_0^3}{k_D} \left(\frac{\pi}{k_0 \rho} \right)^{1/2} e^{-jp} F(p) \right) \end{aligned}$$

$$\begin{aligned}
g_z^v = & \left[\frac{jk_D^2}{r_d} - \frac{k_D}{r_d^2} - \frac{j}{r_d^3} - \left(\frac{z - z'}{r_d} \right)^2 \right. \\
& \times \left. \left(\frac{jk_D^2}{r_d} - \frac{3k_D}{r_d^2} - \frac{3j}{r_d^3} \right) \right] e^{jk_D r_d} \\
& + 2 \frac{jk_0^2}{k_D^2} e^{jk_D r_i} \left(\frac{z + z'}{\rho} \right) \left(\frac{jk_D^2}{\rho} - \frac{k_D}{2\rho^2} + \frac{7j}{8\rho^3} \right) \\
& - e^{jk_D r_i} \left[\frac{jk_D^2}{r_i} - \frac{k_D}{r_i^2} - \frac{j}{r_i^3} - \left(\frac{z + z'}{r_i} \right)^2 \right. \\
& \times \left. \left(\frac{jk_D^2}{r_i} - \frac{3k_D}{r_i^2} - \frac{3j}{r_i^3} \right) \right] \\
& + 2 \frac{k_0^2}{k_D^2} e^{-jk_D(z+z')} e^{jk_0 \rho} \\
& \times \left(\frac{jk_0^2}{\rho} - \frac{k_0}{\rho^2} - \frac{j}{\rho^3} - \frac{k_0^4}{k_D} \left(\frac{\pi}{k_0 \rho} \right)^{1/2} e^{-jp} F(p) \right) \\
F(p) = & \frac{1}{2} (1 + j) - \int_0^p \frac{1}{\sqrt{2\pi t}} e^{jt} dt, \quad p = \frac{k_0^3 \rho}{2k_D^2}. \quad (15)
\end{aligned}$$

Although (15) is expressed in integral form, its range is limited by the maximum and minimum values of ρ so that (15) can be easily approximated via a polynomial interpolation or tabulated.

These formulas are valid under the following conditions:

$$|k_D| \geq 3k_0 \quad |k_D \rho| > 3. \quad (16)$$

If these conditions are not met, the lateral wave contribution diverges. In these isolated cases, the homogeneous Green's function for the direct and reflected waves can be used [8]–[10].

The advantage of using this formulation rather than the spectral representations [8], [9] is that the Green's function

computation time for each $(\mathbf{r}, \mathbf{r}')$ pair is comparable with the case of free space since the expressions, although lengthy, are still in closed form.

ACKNOWLEDGMENT

The authors would like to thank Mr. W. J. Baldygo, Air Force Research Laboratory, and Dr. J. A. Sjogren, Air Force Office of Scientific Research, for sponsoring this research.

REFERENCES

- [1] L. Lo Monte, D. Erricolo, F. Soldovieri, and M. C. Wicks, "Radio frequency tomography for tunnel detection," *IEEE Trans. Geosci. Remote Sens.*, vol. 48, no. 3, pp. 1128–1137, Mar. 2010.
- [2] J. Norgard, M. C. Wicks, and A. Drozd, "Distributed/embedded subsurface sensors for imaging buried objects with reduced mutual coupling and suppressed electromagnetic emissions," in *Proc. ICEAA*, Turin, Italy, Sep. 17–21, 2007, pp. 427–430.
- [3] T. J. Cui and W. C. Chew, "Diffraction tomographic algorithm for the detection of three-dimensional objects buried in a lossy half-space," *IEEE Trans. Antennas Propag.*, vol. 50, no. 1, pp. 42–49, Jan. 2002.
- [4] G. Leone and F. Soldovieri, "Analysis of the distorted born approximation for subsurface reconstruction: Truncation and uncertainties effect," *IEEE Trans. Geosci. Remote Sens.*, vol. 41, no. 1, pp. 66–74, Jan. 2003.
- [5] P. Meincke, "Linear GPR inversion for lossy soil and a planar air-soil interface," *IEEE Trans. Geosci. Remote Sens.*, vol. 39, no. 12, pp. 2713–2721, Dec. 2001.
- [6] A. Giannopoulos, GPRMAX Simulator. [Online]. Available: www.gprmax.org
- [7] M. S. Zhdanov, *Geophysical Inverse Theory and Regularization Problems, Methods in Geochemistry and Geophysics*, vol. 36. Amsterdam, The Netherlands: Elsevier, 2002.
- [8] W. C. Chew, *Waves and Fields in Inhomogeneous Media*. Piscataway, NJ: IEEE Press, 1995.
- [9] C. T. Tai, *Dyadic Green Functions in Electromagnetic Theory*, 2nd ed. Piscataway, NJ: IEEE Press, 1993.
- [10] R. W. P. King, M. Owens, and T. T. Wu, *Lateral Electromagnetic Waves*. New York: Springer-Verlag, 1992.
- [11] P. C. Hansen, *Rank Deficient and Discrete Ill-Posed Problems*. Philadelphia, PA: SIAM, 1998.